Biomaterials Translational

Recombinant human bone morphogenetic protein-2–engineered piezoplatform synergistically promotes bone regeneration through bone morphogenetic protein receptor activation

Lijie Mao[1,2], Dong Zhang[1], Zehao Shen[1], Xinqing Wang[1], Chen Lai[3], Fangping Chen[1,4*], and Changsheng Liu[1,4*]

ABSTRACT

Bone morphogenetic protein-2 (BMP-2) is a potent cytokine that promotes bone formation in orthopedic procedures. However, the delivery of recombinant human BMP-2 (rhBMP-2) with sustained release kinetics, while maximizing osteogenic potential, remains a challenge. In this study, we constructed a novel rhBMP-2–engineered piezoplatform for sustained release of rhBMP-2 and synergistic enhancement of osteoinductive activity. The piezoelectric signals are capable of initiating rapid biomineralization and promoting the early adhesion, proliferation, and osteogenic differentiation of bone marrow stromal cells (BMSCs), as well as enabling efficient immobilization and sustained release of rhBMP-2 through electrostatic interactions. Notably, piezoelectric stimulation synergizing with rhBMP-2 enhances osteogenesis-related protein production. This is achieved by amplifying the expression of BMP-2 receptors (*Bmpr1a* and *Bmpr2*) in BMSCs by approximately three-fold, which in turn reinforces the regenerative capacity of rhBMP-2. The rat femur defect model further confirms the osteogenic efficacy of the rhBMP-2–engineered piezoplatform. These findings are expected to advance the development of biopiezoelectric implants incorporating growth factor therapy for tissue engineering.

Keywords:
Bone morphogenetic protein receptors; Bone regeneration; Piezoelectric stimulation; Recombinant human bone morphogenetic protein-2

***Corresponding authors:**
Fangping Chen, fpchen@ecust.edu.cn;
Changsheng Liu, liucs@ecust.edu.cn

How to cite this article:
Mao L, Zhang D, Shen Z, *et al.* Recombinant human bone morphogenetic protein-2–engineered piezoplatform synergistically promotes bone regeneration through bone morphogenetic protein receptor activation. *Biomater Transl.* 2025, 6(4), 450-464.

doi: 10.12336/bmt.25.00019

1. Introduction

Recombinant human bone morphogenetic protein-2 (rhBMP-2), a critical growth factor with osteoinductive properties, has been approved for clinical use due to its potent ability to induce osteogenesis and bone formation.[1] However, rhBMP-2 has a short half-life (only 7–16 min) in the bloodstream,[2] and its osteogenic effects are highly dependent on its release rate and dosage from scaffolds. Moreover, burst release or supraphysiological dosages of rhBMP-2 typically lead to inflammatory responses, heterotopic ossification, and bone cyst formation, posing a significant challenge to its clinical application.[3,4] Therefore, encapsulating rhBMP-2 within scaffolds is of utmost importance for protecting it, prolonging its bioactivity, and controlling cellular activities at defect sites.

In recent years, significant efforts have been made to immobilize rhBMP-2 and control its release through covalent immobilization and electrostatic adsorption to fully utilize its osteogenic potential by prolonging Smad signaling activation.[5-7] In our previous studies, we demonstrated that sulfonated gelatin hydrogels facilitate a sustained release of rhBMP-2 due to the negatively charged sulfonation groups within the hydrogel, which allow for

stronger binding to rhBMP-2.[1,8] Bone itself is a piezoelectric tissue, in which collagen fibers, oriented and aligned under physiological load, generate electrical signals and an electric microenvironment.[9] To date, little attention has been paid to the effect of piezoelectric signaling on the immobilization, conformation, and biological activity of rhBMP-2. In addition, how piezoelectric signaling influences the osteogenic activity of rhBMP-2, and the potential synergistic effects between rhBMP-2 and electrical signaling on osteogenesis, remain largely unexplored. Therefore, exploring the synergistic effect of piezoelectric scaffolds with rhBMP-2 may be crucial for improving the efficacy of bone regeneration.

Materiobiology aims to modulate the microenvironment of the target extracellular matrix to confer new or enhanced cellular functions by leveraging the biophysical properties of biomaterials.[10] Therefore, recapitulating the electric microenvironment around the defect site through the implantation of scaffolds is an alternative strategy to achieve optimal bone regeneration. Piezoelectric ceramics, such as barium titanate (BT), have attracted considerable interest in biomedical applications for their excellent mechanical properties, force-to-electricity conversion capability, and favorable biocompatibility.[11-13] Electrical stimulation of BT/tricalcium phosphate (TCP) scaffolds is favorable for enhancing biomineralization and increasing intracellular Ca^{2+} concentration in bone marrow stromal cells (BMSCs), which ultimately promotes their osteogenic differentiation through focal adhesion kinase/extracellular signal-regulated kinase and BMP/Smad signaling cascades.[14] In addition, BT coating on Ti6Al4V scaffolds has been reported to promote anti-inflammatory polarization of macrophages by inhibiting mitogen-activated protein kinase/c-Jun N-terminal kinase and promoting oxidative phosphorylation, thereby enhancing bone regeneration in a sheep cervical corpectomy model.[15] In this regard, a piezoelectric BT scaffold with efficient immobilization and controlled delivery of rhBMP-2 provides an effective platform for amplifying its osteogenic effects and achieving synergistic bone repair.

In this study, porous piezoelectric scaffolds consisting of piezoelectric BT and bioactive β-TCP (P-BTCP) were constructed through a polyurethane template sacrificial method. Then, rhBMP-2 was loaded onto scaffolds (P-BTCP/BMP-2) by freeze-drying for targeted delivery and controlled release (**Figure 1**). After characterization of the intrinsic scaffold properties, we evaluated the biomineralization and early cellular behavioral responses of P-BTCP. Subsequently, the protein adsorption, release kinetics, secondary structure, and osteogenic capacity of rhBMP-2 on P-BTCP were measured.

Furthermore, the synergistic effects of electrical stimulation and rhBMP-2 on cellular functions were investigated, including the proliferation, migration, and osteogenic activities of BMSCs. Moreover, the underlying mechanism by which electrical stimulation and rhBMP-2 synergistically promote osteogenesis was explored. Finally, a rat weight-bearing femur defect model was developed to investigate the *in vivo* bone regeneration capacities of P-BTCP/BMP-2. These findings suggest that piezoelectric stimulation concomitantly initiates early-stage bone healing and enhances the regenerative capacity of rhBMP-2, providing an effective strategy for hard tissue regeneration mediated by rhBMP-2.

2. Materials and methods

2.1. Scaffold fabrication

The three-dimensional (3D) BTCP scaffolds were fabricated using a polyurethane template. The P-BTCP was then obtained in an external electric field generated by a piezoelectric polarization device (PZT-FJH20/3, Jingke Co. Ltd, China). The scaffold without polarization was termed non-piezoelectric BTCP (N-BTCP).

Briefly, TCP was prepared through chemical precipitation,[16] and BT powders were obtained from Aladdin Co., China. Hierarchical BTCP scaffolds (Φ10.0 × 10.0 mm^3 for mechanical tests; ϕ10.0 × 2.0 mm^3 for *in vitro* cell experiments; Φ3.0 × 4.0 mm^3 for *in vivo* assessments) were fabricated using the polyurethane template method (**Figure 2A**). TCP (2 g) and BT (8 g) were added to a 10 mL polyvinyl alcohol solution (10 wt% in water), followed by continuous stirring to obtain a homogeneous slurry. The polyurethane sponge, pre-shaped as required, was then fully saturated with the slurry and repeatedly squeezed to ensure a uniform coating. After drying at 60°C for 72 h, porous BTCP scaffolds were obtained, followed by calcination in a resistance furnace using a rate-controlled two-step sintering process (Figure S1).

The prepared BTCP scaffold was then polarized with a 6 kV/mm direct current electric field for 20 min under ambient conditions to obtain P-BTCP.

2.2. Characterization of P-BTCP scaffolds

The surface morphology, elemental distribution, average pore diameter, and ferroelectric domain structures of P-BTCP scaffolds were characterized using a field emission scanning electron microscope (FE-SEM; S-4800, Hitachi, Japan) and energy dispersive spectroscopy (EDS; IE 300 X, Oxford Instruments, Britain). The porosity of P-BTCP scaffolds was determined using the pycnometer method and calculated based on Equation (1):

$$Porosity(\%) = \frac{W_0 + W_1 - W_2}{W_1 - W_3} \times 100\% \quad (1)$$

where W_0 and W_1 are the mass of dry P-BTCP and the pycnometer filled with water, respectively. After hanging the

[1]Engineering Research Center for Biomedical Materials of Ministry of Education, East China University of Science and Technology, Shanghai, China; [2]Shanghai Tenth People's Hospital, Shanghai Frontiers Science Center of Nanocatalytic Medicine, School of Medicine, Tongji University, Shanghai, China; [3]Shenzhen Key Laboratory of Human Tissue Regeneration and Repair, PKU–HKUST ShenZhen–HongKong Institution, Shenzhen, Guangdong, China; [4]Key Laboratory for Ultrafine Materials of Ministry of Education, School of Materials Science and Engineering, East China University of Science and Technology, Shanghai, China

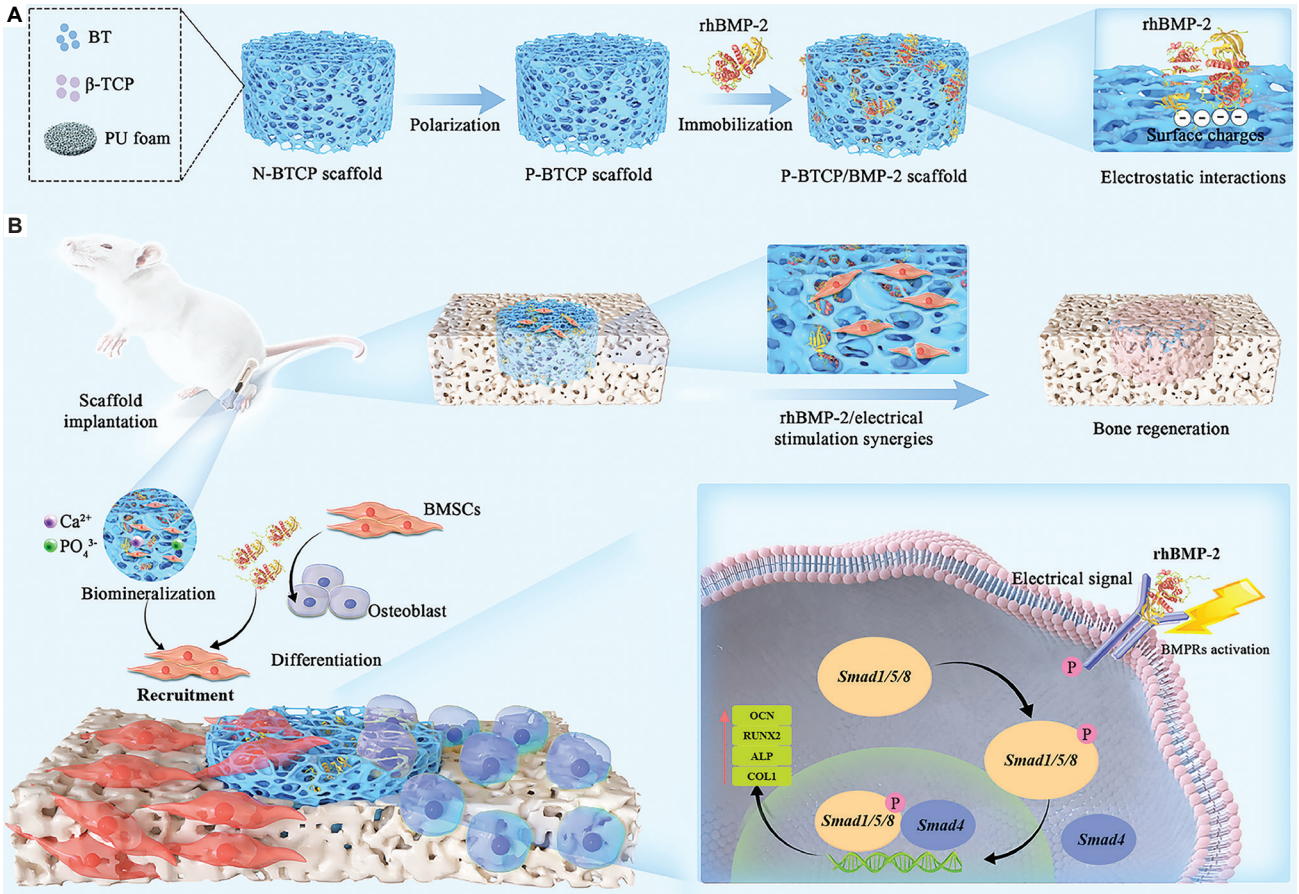

Figure 1. Preparation and mechanism of P-BTCP/BMP-2 scaffold for bone regeneration. (A) Schematic illustration of the preparation of the P-BTCP/BMP-2 scaffold. (B) Mechanism of P-BTCP/BMP-2 scaffolds in repairing rat femur defects. Electrical stimulation from P-BTCP activates BMPR expression in BMSCs and facilitates the binding of rhBMP-2 to BMPRs. The P-BTCP/BMP-2 scaffolds provide efficient immobilization and sustained release of rhBMP-2 through electrostatic interactions, synergistically promoting the osteogenic differentiation of BMSCs in combination with the electrical microenvironment.
Abbreviations: BMPR: Bone morphogenetic protein receptor; BMSC: Bone marrow stromal cell; BT: Barium titanate; N-BTCP: Non-piezoelectric barium titanate/tricalcium phosphate; P-BTCP: Piezoelectric barium titanate/tricalcium phosphate; PU: Polyurethane; rhBMP-2: Recombinant human bone morphogenetic protein-2; TCP: Tricalcium phosphate.

scaffolds in the pycnometer and absorbing the overflow water, the mass of the pycnometer was measured and recorded as W_2. The mass of the pycnometer after removing the scaffolds was recorded as W_3.

The phase composition and crystallographic information of P-BTCP were determined using an X-ray diffractometer (D/max2550VB/PC, RIGAKU, Japan). The mechanical properties of the scaffolds were evaluated using a universal testing machine (CMT2503, MTS, United States [USA]) with a loading speed of 1 mm/min. Five specimens were tested, and the average modulus was calculated. After polarization, the piezoelectric constant (d_{33}) of P-BTCP was assessed using a quasi-static d_{33} apparatus (ZJ-3A, Chinese Academy, China).

The pH values after soaking N-BTCP and P-BTCP in phosphate-buffered saline (PBS) were measured. N-BTCP and P-BTCP scaffolds were immersed in PBS separately at a scaffold-to-PBS ratio of 0.01 g/mL. The pH of the medium was measured using a pH electrode (Five Easy PlusTM pH meter, METTLER TOLEDO, USA) at specified intervals.

2.3. Bioactivity of scaffolds *in vitro*

In vitro bioactivity was evaluated by immersing N-BTCP and P-BTCP scaffolds in simulated body fluid (SBF) with a weight-to-volume ratio of 0.01 g/mL.[17] Fresh medium was replaced every other day for 3, 7, and 14 days. Afterward, the scaffolds were removed, rinsed 3 times with deionized water, and dried at 37°C for 48 h. The elemental compositions of porous scaffolds were evaluated using scanning electron microscopy (SEM)–EDS.

2.4. Cell isolation and cell culture

Rat BMSCs were isolated from Sprague–Dawley rats (male; n = 5; Shanghai Jiesijie Experimental Animal Co., Ltd, China). Cells were cultured in α-minimum essential medium (α-MEM; Thermo Fisher Scientific, United States), supplemented with 10% fetal bovine serum (FBS; Thermo Fisher Scientific, Australia) and 1% penicillin–streptomycin (Beyotime, China), in a humidified atmosphere of 5% carbon dioxide at 37°C. The culture medium was refreshed every 3 days. Upon reaching

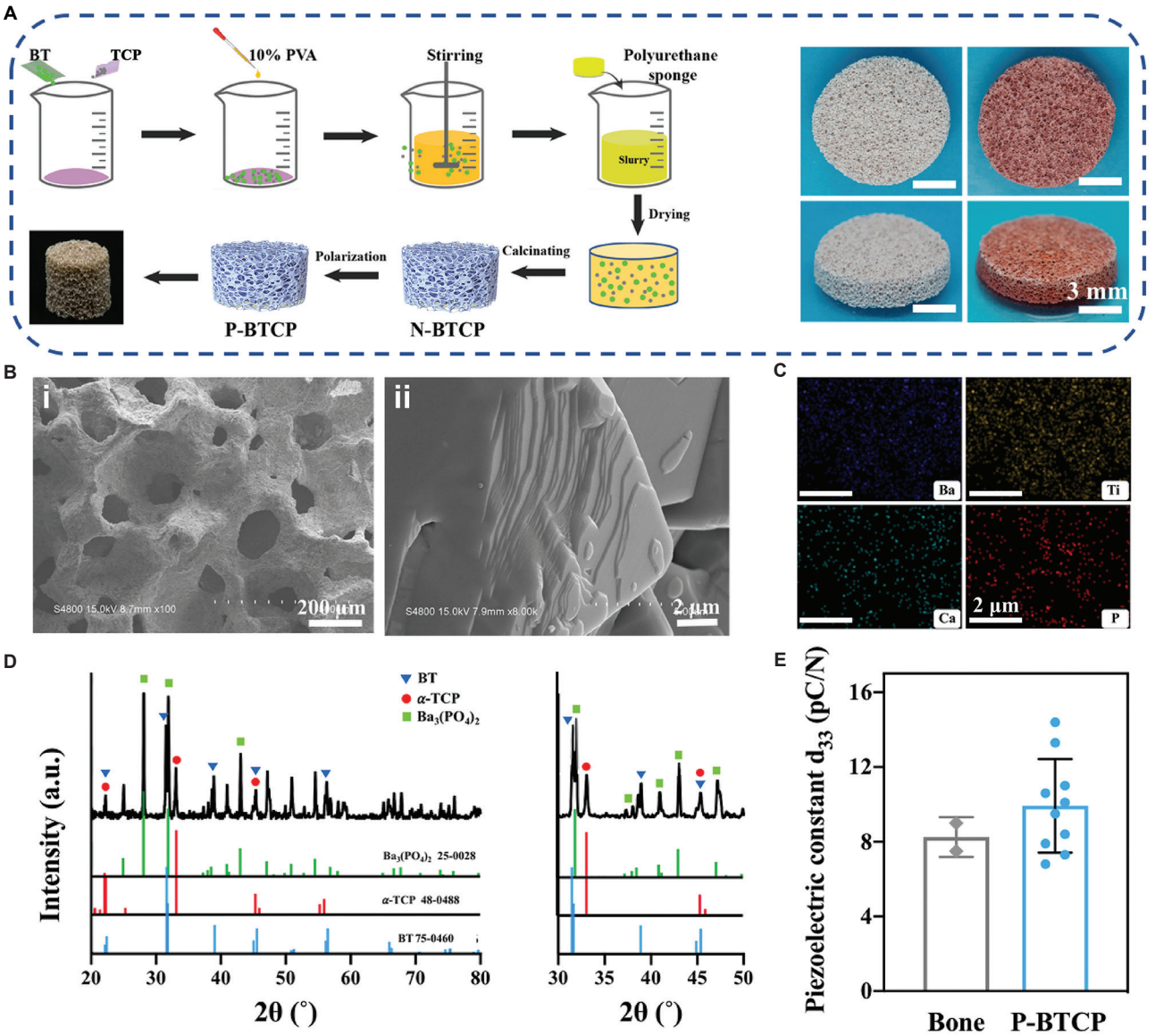

Figure 2. Characterization of the scaffolds. (A) Schematic illustration of the preparation and digital images of N-BTCP and P-BTCP scaffolds (scale bar: 3 mm). (B) SEM images of the (i) surface topography (scale bar: 200 μm; magnification: 100×) and (ii) electric domains (scale bar: 2 μm; magnification: 8,000×) of P-BTCP scaffolds. (C) SEM–EDS micrographs showing surface element mapping of P-BTCP scaffolds (scale bar: 2 μm; magnification: 8,000×). (D) XRD patterns and phase compositions of P-BTCP after sintering at 1,400℃. (E) Piezoelectric constants (d_{33}) of natural bone and P-BTCP.

Abbreviations: BT: Barium titanate; EDS: Energy dispersive spectroscopy; N-BTCP: Non-piezoelectric barium titanate/tricalcium phosphate; P-BTCP: Piezoelectric barium titanate/tricalcium phosphate; PVA: Polyvinyl alcohol; SEM: Scanning electron microscopy; TCP: Tricalcium phosphate; XRD: X-ray diffraction.

80–90% confluency, BMSCs were detached using 0.25% trypsin. For *in vitro* cell experiments, BMSCs at passages 3–5 were used.

2.5. Cell adhesion and viability on scaffolds

All scaffolds were steam sterilized at 121°C and 1.21 MPa for 30 min. To investigate the biocompatibility of the scaffolds, N-BTCP and P-BTCP were soaked in serum-free α-MEM for 24 h. The supernatant was collected and supplemented with 10% FBS to obtain scaffold-conditioned medium. After BMSCs were incubated overnight, the culture medium was gently removed and replaced with N-BTCP and P-BTCP medium. Cells cultured in normal medium served as a control. Cell viability was measured using the cell counting kit-8 (CCK-8; Dojindo, Japan) assay after 1, 3, and 5 days of culture. Cytocompatibility and proliferation of BMSCs on scaffolds were also measured using the CCK-8 assay after incubation on N-BTCP and P-BTCP for 3 days. The optical density (OD) value at 450 nm was measured using a microplate reader (Spectra Max 384, Molecular Devices, USA).

Cell adhesion of BMSCs on scaffolds was observed using FE-SEM after 24 h of incubation. Briefly, the culture medium was carefully removed, followed by washing with PBS twice. Then, the samples were fixed with 2.5% glutaraldehyde for 15 min and serially dehydrated with gradient ethanol (30%, 50%,

70%, 80%, 90%, and 100% v/v) for 3–5 min at each step. After immersion in isoamyl acetate and air-drying at 37°C overnight, the samples were sputter-coated with gold, and cell morphology was observed using FE-SEM. For better observation of cellular infiltration into scaffolds, the samples were fixed and stained with fluorescein isothiocyanate. Confocal laser-scanning microscopy (CLSM; A1R, Nikon, Japan) was employed to visualize the morphology of cells infiltrating the scaffolds.

2.6. Protein and rhBMP-2 adsorption on scaffolds

A bicinchoninic acid (BCA) assay kit (P0010, Beyotime, China) was used to measure bovine serum albumin (BSA) adsorbed onto the BTCP scaffolds. N-BTCP and P-BTCP were immersed in BSA solutions at different concentrations (0, 0.5, 1, 2, 4, 8, and 16 mg/mL) for 2 h, and the supernatant was then collected to measure the residual BSA concentration. The protein mass was quantified by measuring absorbance at 562 nm, using a standard curve for reference.

The scaffolds were immersed in 8 mg/mL BSA solutions for 2 h, followed by lyophilization to obtain BSA-loaded N-BTCP and P-BTCP scaffolds. They were then placed in 1 mL of PBS and incubated on a shaking platform at 37°C. At predetermined intervals, 20 μL of supernatant was collected and replenished with an equivalent volume of fresh PBS. The BSA concentration of each collected sample was measured using the BCA assay to calculate the released amount.

A human BMP-2 enzyme-linked immunosorbent assay (ELISA; 900-K255K, Thermo Fisher Scientific, United States) kit was used to measure rhBMP-2 adsorption. In brief, sterilized N-BTCP and P-BTCP scaffolds were immersed in 100 μL of 0.25 mg/mL rhBMP-2 (Shanghai Rebone Biomaterials Co. Ltd., China) solution at 4°C for 24 h. The supernatant was removed and kept for the ELISA assay, and the scaffolds were washed twice with PBS to remove the non-adsorbed rhBMP-2. After aseptic lyophilization, rhBMP-loaded N-BTCP (N-BTCP/BMP-2) and rhBMP-loaded P-BTCP (P-BTCP/BMP-2) scaffolds were obtained.

The N-BTCP/BMP-2 and P-BTCP/BMP-2 scaffolds used in animal experiments were prepared using the same method. The ratio of rhBMP-2 to scaffold was 1 mg/g in the rat femoral defect model.

2.7. Bioactivity of rhBMP-2 released from scaffolds

Secondary structures of the released rhBMP-2 were investigated by suspending N-BTCP/BMP-2 and P-BTCP/BMP-2 scaffolds in 500 μL PBS and maintaining them at 4°C for 24 h. The solutions were collected and analyzed using circular dichroism (CD) measurements (JASCO J-715, Shimadzu, Japan). The secondary structures of free rhBMP-2 and released rhBMP-2 were estimated using the CD spectra deconvolution software, CDNN (CDNN 2.1, Applied Photophysics Ltd, United Kingdom).

Alkaline phosphatase (ALP) activity was further examined to evaluate the bioactivity of scaffold-released rhBMP-2. BMSCs were cultured with both scaffold-released rhBMP-2 and free rhBMP-2. After 7 days, the cells were lysed in NP-40 lysis buffer, followed by the addition of the ALP working solution according to the manufacturer's protocol. The OD was subsequently measured at 405 nm. Furthermore, the relative ALP activity was normalized to the total protein content of the cells, which was determined using the BCA Assay Kit. Moreover, ALP staining was performed after 7 days of incubation using the BCIP-NBT kit (C3206, Beyotime, China) and observed with a light microscope (TE2000U, Nikon, Japan).

2.8. Bioactivity of rhBMP-2–engineered scaffolds *in vitro*

Cytocompatibility of rhBMP-2–engineered scaffolds was measured using CCK-8 after incubation of BMSCs on the scaffolds for 3 days. BMSCs attached to the rhBMP-2–engineered scaffolds were observed using FE-SEM after 24 h incubation, whereas cellular infiltration into the scaffolds was visualized using CLSM.

Cell recruitment was further assessed using an 8 μm transwell cell-culture plate, which featured a permeable polycarbonate membrane separating the upper and lower compartments. Briefly, BMSCs were seeded into the upper chamber containing 400 μL of serum-free α-MEM, and the scaffolds were placed into the lower chamber with 600 μL of α-MEM supplemented with 10% FBS. After 24 h of incubation, the cells that migrated to the lower chamber were fixed and stained with 0.5% crystal violet for 20 min. Cells recruited to the bottom chamber were visualized under a light microscope, and cell numbers were quantified using ImageJ software (ImageJ 1.53a, Wayne Rasband, United States).

2.9. Osteogenesis of rhBMP-2–engineered scaffolds *in vitro*

Expression of BMP receptor (BMPR) genes (e.g., *Bmpr1a*, *Bmpr1b*, and *Bmpr2*) and osteogenesis-related genes (e.g., *Smad1*, *Smad4*, *Smad5*, *Smad8*, *Osx*, *Runx2*, and *Col1a1*) in BMSCs was evaluated using quantitative reverse transcription polymerase chain reaction (qRT-PCR) after 3 days of incubation on rhBMP-2–engineered scaffolds. Briefly, total cellular RNA was extracted using Trizol reagent, and its concentration was assessed by measuring the absorbance at 260 and 280 nm using an ultra-micro ultraviolet spectrophotometer (NanoDrop One, Thermo Fisher Scientific, USA). Total cellular RNA was converted into cDNA using the iScriptTM cDNA Synthesis Kit (1708890, BIO-RAD, United States). cDNA, together with iTaqTM Universal SYBR® Green Supermix (BIO-RAD, United States), was subjected to qRT-PCR. The relative gene expression levels were calculated based on the $2^{-\Delta\Delta Ct}$ method, with *Gapdh* serving as the housekeeping gene. The sequences of primers for all target genes are listed in Table S1.

To evaluate ALP activity, BMSCs were seeded on rhBMP-2–engineered scaffolds for 7 days. ALP staining was performed and visualized under a light microscope. In addition, mineralization of the extracellular matrix was measured with alizarin red staining after 14 days of culture. Briefly, 500 μL alizarin red staining solution was added and incubated in the dark for 5–10 min, after which images were captured by a light microscope.

Osteogenesis-related proteins (e.g., RUNX2, OCN, COL1, OSX, SMAD1/5/9) expression and localization were evaluated through Western blot. It is noteworthy that *Smad9* is the formal name for the gene previously known as *Smad8*. After BMSCs were cultured on the scaffolds for 3 days, proteins were extracted using radioimmunoprecipitation lysis with 1 mM phenylmethanesulfonyl fluoride. The extracted protein was separated using 10% sodium dodecyl sulfate–polyacrylamide gel electrophoresis, followed by transfer to a polyvinylidene difluoride membrane. The membrane was subsequently blocked with 5% BSA and incubated overnight at 4°C with primary monoclonal antibodies. Afterward, the horseradish peroxidase-conjugated secondary antibody (ab6721, Abcam, United Kingdom) was incubated at room temperature for 2 h. Protein expression was detected using a chemiluminescence imaging system and quantitatively analyzed with ImageJ, with glyceraldehyde-3-phosphate dehydrogenase serving as the loading control.

2.10. Molecular mechanism analysis

To further explore the underlying mechanism by which P-BTCP and rhBMP-2 synergistically facilitate osteogenesis, BMSCs were treated with a small molecule inhibitor, LDN 193189 (Aladdin Scientific, USA), which selectively targets BMP type I receptor kinases, thereby inhibiting BMP signaling through p-Smad5 expression.[18] BMSCs were seeded on N-BTCP/BMP-2 and P-BTCP/BMP-2 scaffolds with or without 0.2 μM LDN 193189 for 3 days. The expression of BMPR proteins (e.g., BMPR1A, BMPR1B, and BMPR2), components of the Smad signaling (e.g., SMAD1, SMAD4, SMAD5, SMAD8), and osteogenesis-related genes (e.g., *Osx*, *Runx2*, *Col1a1*, and *Alpl*) was evaluated using qRT-PCR. In addition, BMPR proteins, Smad proteins, and osteogenesis-related proteins were analyzed using Western blotting.

2.11. *In vivo* evaluation of bone regeneration

Animal experiments were performed following guidelines approved by the Animal Ethics Committee of East China University of Science and Technology (ECUST-21046). Bone regeneration was evaluated using a femur defect model in male Sprague–Dawley rats (age: 12 weeks). Following general anesthesia with 10% chloral hydrate, the fur over both distal femurs of the rats was shaved and disinfected with iodine. Anesthesia was maintained throughout the procedure through inhalation of sevoflurane. A defect measuring 3.0 mm × 4.0 mm (diameter × depth) was created using a low-speed electric drill under sterile normal saline irrigation. Subsequently, the defects were randomly assigned to blank control (CON), N-BTCP, P-BTCP, and P-BTCP/BMP-2 scaffold groups, with six replicates per group. At 4, 8, and 12 weeks, the rats were euthanized with an overdose of anesthetic, and their femurs were collected. The major organs, including the heart, liver, spleen, lungs, and kidneys, were harvested and subjected to pathological analyses for biosafety evaluation of the scaffolds.

The harvested femurs were fixed in 4% paraformaldehyde and analyzed using micro-computed tomography (BL13W, Shanghai Synchrotron Radiation Facility, China). Samples were scanned at a pixel size of 9 μm, and the resulting images were reconstructed into 3D models using Volume Graphics software (VG 3.4.4, Volume Graphics GmbH, Germany). Undecalcified sections were stained with Van Gieson (VG) for microscopic examination of mineralized bone tissue. For hematoxylin and eosin (H&E) staining, the samples were decalcified in 14% ethylenediaminetetraacetic acid and embedded in paraffin for sectioning.

2.12. Statistical analysis

All quantitative data are expressed as the mean ± standard deviation. Statistical significance was determined through one-way analysis of variance followed by Tukey's *post hoc* test using GraphPad Prism version 8.0 software (GraphPad, USA). In all evaluations, differences among groups were considered statistically significant when $p<0.05$.

3. Results and discussion

3.1. Preparation and characterization of scaffolds

Porous BTCP scaffolds were fabricated using a polyurethane sponge as a sacrificial template, and the BT-to-TCP volume ratio was 67:33 (**Figure 2A**). **Figure 2B** displays SEM images of porous P-BTCP scaffolds. The scaffolds exhibited an interconnected macroporous structure with pore sizes of 100–500 μm. The open interconnected porous structure and high surface area of the scaffolds are conducive to stress transmission, nutrient diffusion, cellular proliferation, and tissue regeneration. In addition, the 90° domain patterns indicate the formation of typical tetragonal BT, which mainly contributes to the piezoelectric effect of scaffolds. The BT and TCP were homogeneously mixed, leading to the uniform distribution of Ba, Ti, Ca, and P elements in the scaffolds (**Figure 2C**). The porosity and average pore diameter of the scaffolds were 66.7% and 241.6 μm, respectively (Table S2), which favor cell attachment and scaffold degradation. Meanwhile, the mechanical properties of P-BTCP scaffolds were significantly improved by BT. The ultimate compressive strength and compressive modulus were 0.5 MPa and 39.3 MPa, respectively, significantly higher than TCP porous scaffolds.[19] The strengthened mechanical properties of the porous P-BTCP scaffolds are mainly due to the uniform arrangement of BT and TCP particles and their continuous network structure (**Figure 2C**).

Figure 2D shows the X-ray diffraction patterns of P-BTCP scaffolds. The peaks at $2\theta = 45.3°$ show a pronounced doublet asymmetric splitting, suggesting the formation of a well-crystallized tetragonal perovskite phase of BT (JCPDF 75-0460). Meanwhile, TCP was converted into α-TCP (JCPDF 48-0488) after sintering at 1,400°C. Interestingly, the peaks at $2\theta = 28.0°$, 31.9°, 43.0°, and 54.5° in the BTCP spectra were attributed to barium phosphate ($Ba_3[PO_4]_2$) according to JCPDF 25-0028, indicating that the P^{5+} entered the BT lattice and replaced Ti^{4+}, forming solid $Ba_3(PO_4)_2$ after sintering.

The phase fractions of $Ba_3(PO_4)_2$ were further determined by fitting the diffraction peaks of $Ba_3(PO_4)_2$ and BT. The weight fractions of $Ba_3(PO_4)_2$ and BT were 51.0% and 43.6%,

respectively, indicating that $Ba_3(PO_4)_2$ was the main phase in BTCP. It has been reported that the density of BT ceramics is significantly increased after doping with P^{5+}.[20] With increased density, the grain gaps in BTCP scaffolds decrease, and the grain size increases, which promotes the formation of electric domain structures and further improves the piezoelectric properties of P-BTCP scaffolds. Based on quasi-static d_{33} measurements, the piezoelectric coefficient (d_{33}) of P-BTCP scaffolds was 10 pC/N (**Figure 2E**), which is similar to that of natural bone (7.5–9 pC/N).[21] The piezoelectric properties of the 3D porous P-BTCP scaffolds were approximately four-fold higher than those reported previously.[22,23] The results further indicate that the formation of $Ba_3(PO_4)_2$ in P-BTCP scaffolds was conducive to effective stress transfer and enhancement of the overall piezoelectric effect.

3.2. Biomineralization and biocompatibility of scaffolds

After immersion in SBF for 3, 7, and 14 days, the surface morphology of BTCP scaffolds was observed using SEM (**Figure 3A**). The findings reveal that fine, granule-shaped precipitates formed on the P-BTCP surface after 3 days of immersion. The precipitates gradually grew into crystal clusters and eventually formed mineralized layers after 7 days of immersion. As the immersion time reached 14 days, the crystal clusters on the P-BTCP surface continued to grow and developed into large mineralized deposits. However, only a few granule-shaped precipitates and crystal clusters formed on the N-BTCP surface after mineralization for 7 and 14 days, respectively. The results indicate that minerals were preferentially deposited onto the surface of P-BTCP scaffolds compared with N-BTCP.

In addition, EDS analysis reveals that the Ca/P molar ratio of mineralized deposits on P-BTCP was 1.60, which was close to low-crystallinity, calcium-deficient hydroxyapatite (Figure S2A).[24-26] More Ca^{2+} ions were attracted by the surface charge of P-BTCP piezoelectric scaffolds. When the Ca^{2+} concentration reached the critical value for bone-like apatite nucleation, apatite layers formed spontaneously. Furthermore, the scaffolds generated a weak alkaline microenvironment with

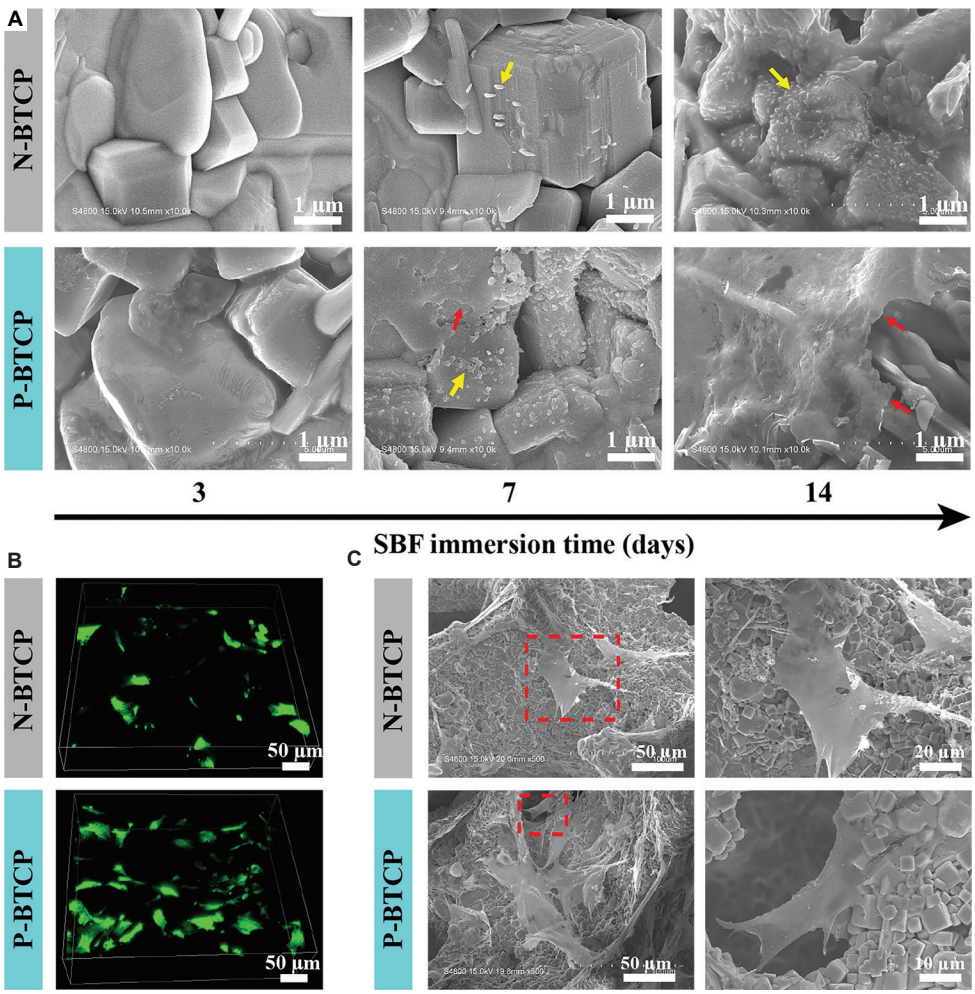

Figure 3. Biomineralization and biocompatibility of scaffolds. (A) *In vitro* mineralization of N-BTCP and P-BTCP after immersion in SBF for 3, 7, and 14 days, with red arrows indicating mineralized layers and yellow arrows indicating crystal clusters (scale bar: 1 μm; magnification: 10,000×). (B) Representative fluorescence microscopy images showing BMSC cellular infiltration into N-BTCP and P-BTCP after incubation for 24 h (scale bar: 50 μm; magnification: 600×). (C) FE-SEM morphology of BMSCs on N-BTCP and P-BTCP, with red dashed boxes indicating the target region for high-magnification observation.
Abbreviations: FE-SEM: Field emission scanning electron microscopy; N-BTCP: Non-piezoelectric barium titanate/tricalcium phosphate; P-BTCP: Piezoelectric barium titanate/tricalcium phosphate; SBF: Simulated body fluid.

pH 7.8 after 1 week of degradation (Figure S2B), synergistically stimulating the spontaneous formation of apatite layers on the P-BTCP and consequently promoting osteoblast viability and bioactivity.

To explore the effect of BTCP scaffolds on BMSCs, cell adhesion was assessed using 3D fluorescence imaging after 24 h of culture (**Figure 3B**). Fluorescence imaging reveals that a greater number of cells penetrated more extensively into the P-BTCP porous scaffolds and attached well along the macropore walls compared to cells on N-BTCP, consistent with the findings from quantitative analysis (Figure S3).

Figure 3C displays the morphology of BMSCs. The results indicate that on both N-BTCP and P-BTCP scaffolds, cells spread out and exhibited good morphology after 24 h of culture. However, cell density and extended pseudopods on P-BTCP scaffolds were significantly higher than on N-BTCP. Moreover, SEM at high magnification showed that the cells bridged across the pores of the P-BTCP scaffolds. In addition, the pseudopods were fully extended and tightly bound to the P-BTCP surface. These findings further confirm that P-BTCP has a stronger ability to enhance cell adhesion than N-BTCP, likely due to the electrical charges on P-BTCP that stimulate the cells to form strong adhesion to the scaffold surface.[25]

In vitro biocompatibility of N-BTCP and P-BTCP was evaluated using a CCK-8 assay. After 3 days of incubation, a higher level of cell proliferation was observed on P-BTCP than on N-BTCP (Figure S2C). Furthermore, the proliferation of BMSCs in scaffold-conditioned medium was similar to that observed in the control group from day 1 to day 5 (Figure S2D).

These findings suggest that the P-BTCP piezoelectric scaffold selectively enhanced the adhesion and proliferation of BMSCs, consistent with previous studies reporting that electrical stimulation can mimic natural bioelectricity to modulate diverse biological functions, ranging from cell-cycle regulation, migration, and proliferation to the differentiation of stem cells.[27]

3.3. *In vitro* protein release kinetics and osteogenic capacity

Bovine serum albumin was selected as a model protein to investigate the protein adsorption behavior of BTCP scaffolds. After immersing in an 8 mg/mL BSA solution for 2 h, the amount of BSA adsorbed on N-BTCP and P-BTCP reached saturation (**Figure 4A**). The protein adsorption capacity of P-BTCP was 0.25 mg of protein/mg of scaffold, almost twice that of N-BTCP (0.13 mg of protein/mg of scaffold). This indicates that the electrically modified P-BTCP surface had a two-fold higher protein adsorption affinity than the N-BTCP surface, suggesting that P-BTCP scaffolds have greater potential for enhancing cell adhesion.

The BSA release curves (**Figure 4B**) exhibited a typical two-stage release of BTCP/BSA scaffolds: an initial burst release within the first six hours, followed by a slow, sustained release. Initially, the protein diffuses through the porous matrix, and the protein exposed on the scaffold surface is easily washed out in water.

After an initial release of approximately 11%, the release rate of BSA from P-BTCP scaffolds became slow and relatively stable, with a cumulative release of 16% over 7 days. The BSA release profile from P-BTCP was more easily controlled than that from N-BTCP. In general, the protein release kinetics from scaffolds are largely affected by pore structures and protein–scaffold interactions.[28,29] The similar initial burst release in

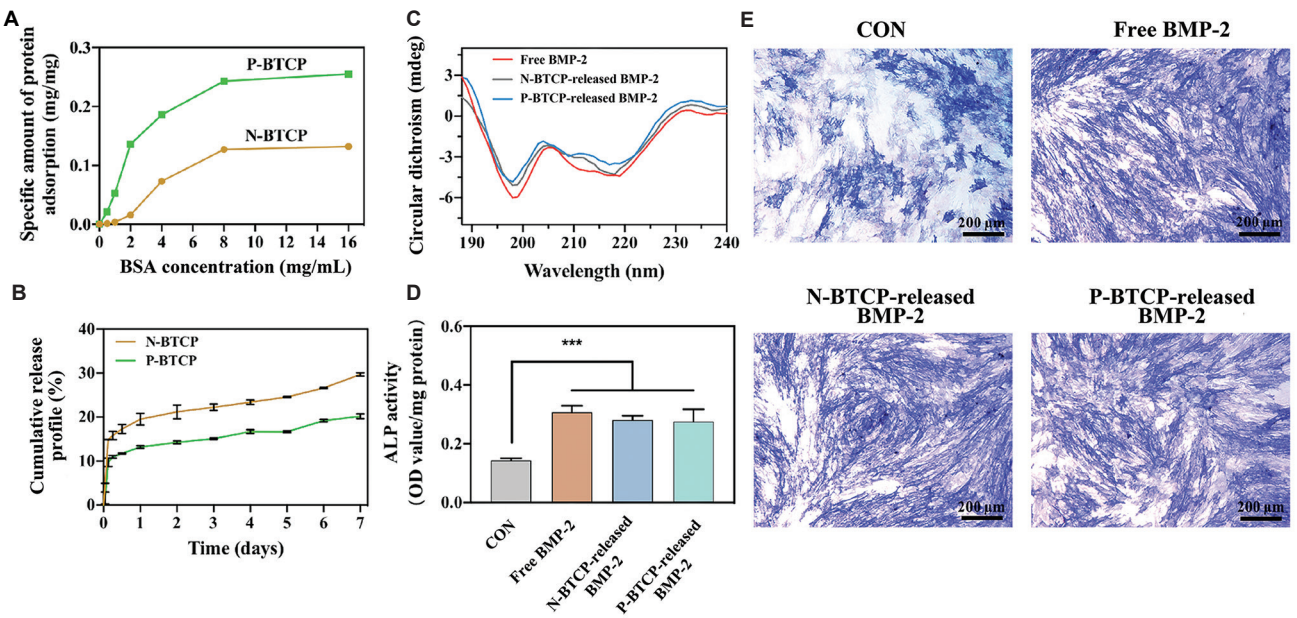

Figure 4. Characterization of protein behavior on scaffolds. (A) Adsorption–concentration curves of BSA on N-BTCP and P-BTCP scaffolds. (B) Cumulative release profiles of BSA from N-BTCP and P-BTCP scaffolds. (C) Circular dichroism spectra, (D) ALP activity, and (E) ALP staining of free BMP-2 and BMP-2 released from scaffolds (scale bar: 200 μm; magnification: 100×). ***$p<0.001$.
Abbreviations: ALP: Alkaline phosphatase; BMP-2: Bone morphogenetic protein-2; BSA: Bovine serum albumin; CON: Control; N-BTCP: Non-piezoelectric barium titanate/tricalcium phosphate; OD: Optical density; P-BTCP: Piezoelectric barium titanate/tricalcium phosphate.

N-BTCP and P-BTCP scaffolds is attributed to macropores, which provide channels for water penetration. In contrast, the slow sustained release of BSA from P-BTCP may be due to the strong electrostatic interaction between BSA and the surface charges of P-BTCP scaffolds, which ensures sustained and effective osteogenic effects of the growth factor or protein *in vivo*.

The secondary structures of rhBMP-2 released from the scaffolds and of free rhBMP-2 were characterized using CD (**Figure 4C**) and structural analyses (**Table 1**). Compared to free rhBMP-2, a slight degree of unfolding, especially a loss of α-helix and β-sheet/turn structures, was observed in the rhBMP-2 released from scaffolds. Notably, the secondary structures of rhBMP-2 released from N-BTCP and P-BTCP were well maintained—only 3.67% and 7.07% changes in secondary structure, respectively. This preservation is mainly attributed to the scaffold pore structure and non-covalent adsorption, which provide sufficient space for conformational flexibility of rhBMP-2.

The results of ALP activity (**Figure 4D**) and ALP staining (**Figure 4E**) further indicate that rhBMP-2 released from scaffolds exhibits osteogenic activity comparable to that of free rhBMP-2. These results suggest that scaffold polarization exerted a negligible influence on rhBMP-2 structure and osteogenic activity. Furthermore, an appropriate electric charge density of scaffolds plays a crucial role in augmenting rhBMP-2–induced osteoblast differentiation and enhancing the potency of the growth factor.[30]

3.4. *In vitro* biocompatibility of rhBMP-2–engineered scaffolds

The biocompatibility of rhBMP-2–engineered piezoelectric scaffolds was evaluated by assessing cellular behaviors such as attachment, cytoskeleton organization, proliferation, and recruitment. Compared to spindle-shaped BMSCs on N-BTCP scaffolds, BMSCs on the N-BTCP/BMP-2 scaffolds displayed a polygonal shape with cellular pseudopodia, an important feature for BMSCs to exhibit high osteogenic activity.[31] Notably, BMSCs on P-BTCP and P-BTCP/BMP-2 scaffolds extended flattened, plate-like processes with abundant filopodia, completely spreading onto the channel walls and forming tight bonds with the P-BTCP and P-BTCP/BMP-2 scaffolds (**Figure 5A**). This finding correlates with that of the CCK-8 assay, as shown in **Figure 5B**. P-BTCP/BMP-2 displayed a higher OD value than N-BTCP and N-BTCP/BMP-2, indicating that P-BTCP/BMP-2 promoted cell proliferation.

Cell cytoskeleton on scaffolds was evaluated using CLSM. Compared with N-BTCP and N-BTCP/BMP-2, the cells on P-BTCP and P-BTCP/BMP-2 scaffolds exhibited more extensive cytoskeletal structures, more deeply distributed along the pore channels with a fusiform morphology (**Figure 5C**), and a larger cell spread area (**Figure 5D**). Moreover, the cell migration assay showed similar results, demonstrating that the migration ability of BMSCs was significantly enhanced on rhBMP-2–loaded scaffolds, with the number of migrated cells on P-BTCP/BMP-2 approximately two-fold higher than that of the other groups (**Figure 5E** and **F**). These findings further confirm that the P-BTCP/BMP-2 scaffolds possessed superior biocompatibility and were conducive to BMSC adhesion, proliferation, and recruitment. Notably, N-BTCP/BMP-2 and P-BTCP were similar in terms of BMSC adhesion, proliferation, and recruitment, indicating that the piezoelectric scaffolds and, primarily, the surface electrical signals played a vital role in initial cell–material interactions.

3.5. *In vitro* osteoinductivity of rhBMP-2–engineered scaffolds

Effective osteogenesis is one of the most critical processes during bone defect repair. Studies have indicated that bone regeneration can be reinforced by electroactive components due to the osteoinductive properties of piezoelectric scaffolds, which facilitate BMSC adhesion, proliferation, migration, and differentiation.[32,33] However, the potential co-effects of piezoelectric scaffolds and rhBMP-2 in inducing osteogenesis have not been clearly elucidated.

The bioeffects of BTCP/BMP-2 scaffolds on the osteogenic differentiation of BMSCs were evaluated *in vitro*. The response of target cells to rhBMP-2 first requires binding to BMPRs, a process modulated by specific cytokines.[34] Remarkably, BMPR activation, known to guide the osteogenic differentiation of stem cells, was observed in BMSCs during cell culture. **Figure 6A** shows that the expression levels of *Bmpr1a*, *Bmpr1b*, and *Bmpr2* in the P-BTCP group were similar to those in the P-BTCP/BMP-2 group, but were approximately three-fold higher than in the N-BTCP and N-BTCP/BMP-2 groups. Moreover, BMSCs on P-BTCP/BMP-2 exhibited relatively stronger osteogenic potential than those on N-BTCP/BMP-2 scaffolds, which was confirmed by the substantially higher expression of *Smad1*, *Smad4*, *Smad8*, *Runx2*, and *Col1a1*. These findings reveal that surface electrical signaling of piezoelectric scaffolds is a critical switch involved in BMP/Smad-induced osteogenic differentiation of BMSCs and acts synergistically with rhBMP-2 in osteogenesis.

Figure 6B shows that P-BTCP/BMP-2 upregulated the expression of RUNX2, OCN, and COL1, consistent with the increased gene expression. After 7 days of culture, higher ALP levels were detected on N-BTCP/BMP-2 and P-BTCP/BMP-2 (**Figure 6C**). In addition, BMSCs on P-BTCP/BMP-2

Table 1. Secondary structures of free rhBMP-2 and rhBMP-2 released from N-BTCP and P-BTCP

Sample	α-helix (%)	β-sheet (%)	β-turn (%)	Random coil (%)	Structural change (%)
Free rhBMP-2	13.17	25.15	17.32	44.36	0.00
rhBMP-2 released from N-BTCP	11.48	23.52	16.97	48.03	3.67
rhBMP-2 released from P-BTCP	10.04	22.15	16.38	51.43	7.07

Abbreviations: N-BTCP: Non-piezoelectric barium titanate/tricalcium phosphate; P-BTCP: Piezoelectric barium titanate/tricalcium phosphate; rhBMP-2: Recombinant human bone morphogenetic protein-2.

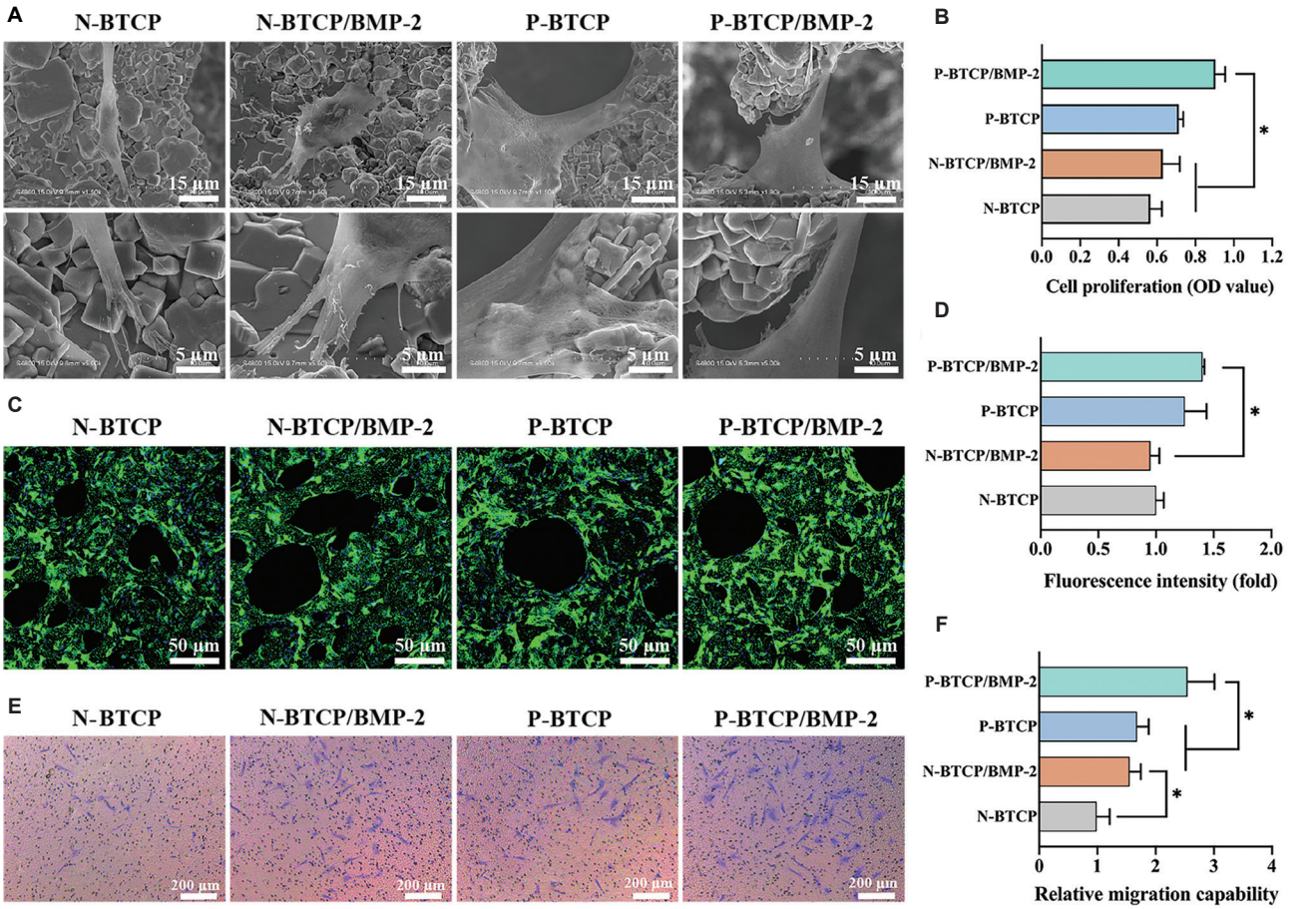

Figure 5. Biocompatibility of rhBMP-2–engineered scaffolds. (A) SEM images of BMSCs after 24 h incubation on N-BTCP, N-BTCP/BMP-2, P-BTCP, and P-BTCP/BMP-2 (scale bar: upper row: 15 μm, magnification: 1,500×; lower row: scale bar: 5 μm; magnification: 5,000×). (B) BMSC proliferation after culturing on the scaffolds for 3 days. (C) CLSM images of BMSCs infiltrating into scaffolds (scale bar: 50 μm; magnification: 600×). (D) Quantitative analysis of the fluorescence intensity of the cytoskeleton. (E) Representative optical images of BMSC migration driven by scaffolds (scale bar: 50 μm; magnification: 100×). (F) Quantitative analysis of recruited BMSCs. *p<0.05.
Abbreviations: BMP-2: Bone morphogenetic protein-2; BMSC: Bone marrow stromal cell; CLSM: Confocal laser-scanning microscopy; N-BTCP: Non-piezoelectric barium titanate/tricalcium phosphate; OD: Optical density; P-BTCP: Piezoelectric barium titanate/tricalcium phosphate; SEM: Scanning electron microscopy.

exhibited the highest osteogenic differentiation (**Figure 6D**). Moreover, extracellular matrix mineralization was assessed by evaluating calcium deposition and mineralization after 21 days of incubation. The differences in the red precipitates indicate the upregulation of calcium nodules in BMSCs on P-BTCP/BMP-2, with approximately two-fold enhancement of mineralization compared to the other groups (**Figure 6E**).

Notably, the extracellular matrix mineralization and osteogenesis-related proteins (RUNX2, OCN, COL1) expressed on P-BTCP were comparable to, or even slightly higher than, those on N-BTCP/BMP-2. Therefore, the electrical microenvironment exerted by P-BTCP induced BMSC osteogenic differentiation by increasing BMPRs expression and initiating BMP/Smad signaling, which in turn promoted extracellular matrix mineralization and triggered the production of a series of osteogenesis-related proteins.

3.6. Mechanism exploration

To further explore the mechanism by which P-BTCP promotes BMSC osteogenesis, BMPRs were inhibited using the small-molecule inhibitor LDN 193189 (**Figure 7A**). The expression of critical genes and proteins within the BMP/Smad signaling pathway was examined. The findings reveal that the expression of *Bmpr1* and *Bmpr2* was effectively suppressed in the P-BTCP/LDN and P-BTCP/BMP-2/LDN groups in the presence of LDN 193189, resulting in a 2–4-fold downregulation of *Smad1/4/5/8* and osteogenesis-related genes (*Osx*, *Alpl*, *Runx2*, and *Col1a1*) (**Figure 7B**). Moreover, the levels of RUNX2 and ALP proteins were markedly attenuated, correlating with inhibition of SMAD1/5/9 phosphorylation (**Figure 7C** and **D**). Taken together, the results confirm that the electrical microenvironment exerted by piezoelectric P-BTCP scaffolds stimulates osteogenesis through activation of BMPRs, which is critical for enhancing the regenerative potential of rhBMP-2 and mitigating the adverse reactions associated with excessive rhBMP-2 dosing.

3.7. *In vivo* bone regeneration of rhBMP-2–engineered scaffolds

The *in vivo* osteogenic efficacy of P-BTCP/BMP-2 scaffolds was investigated in a rat weight-bearing femoral defect model

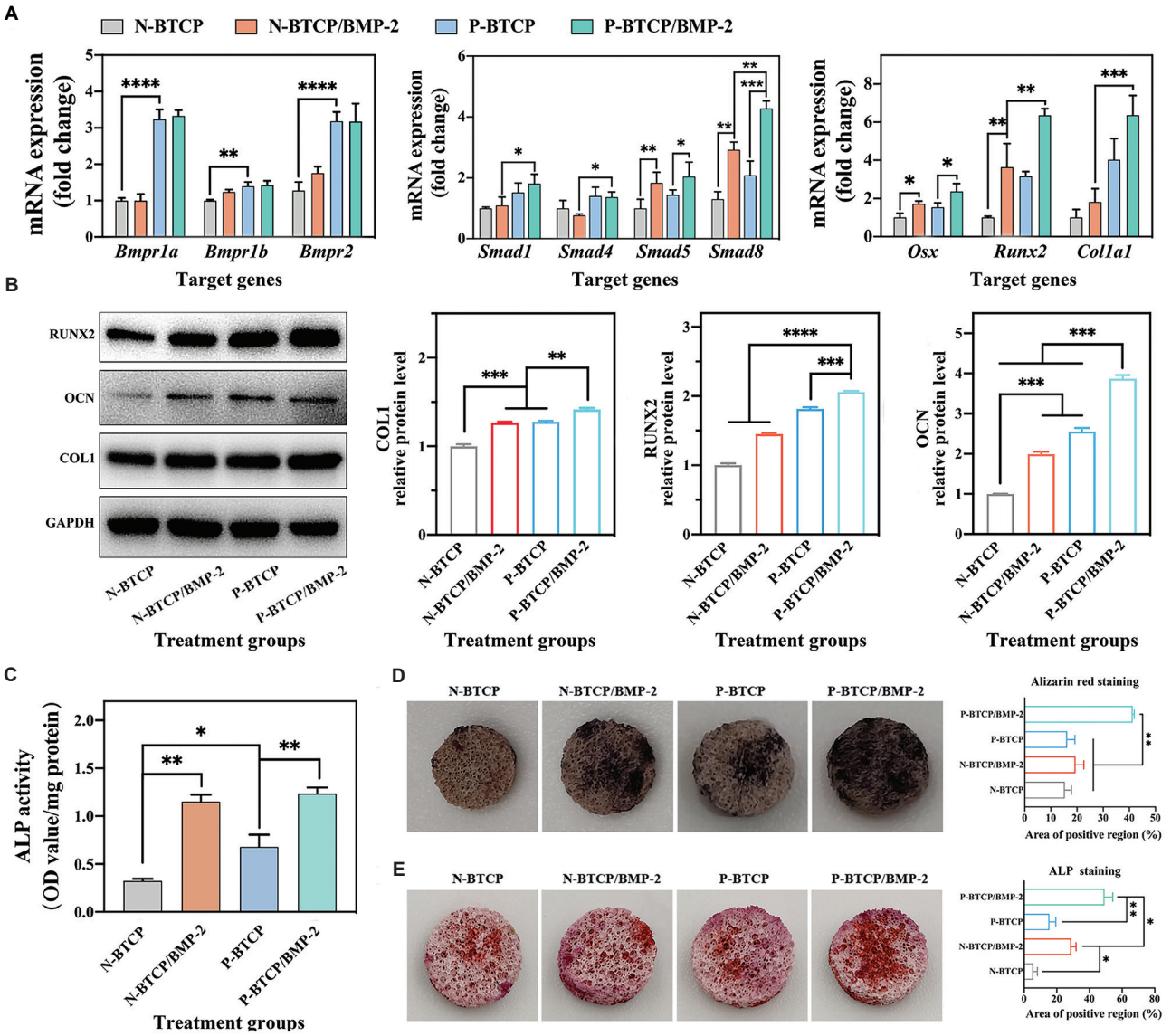

Figure 6. Osteoinductive profile of rhBMP-2–engineered scaffolds. (A) Gene expression of *Bmpr1a*, *Bmpr1b*, *Bmpr2*, *Smad1*, *Smad4*, *Smad5*, *Smad8*, *Osx*, *Runx2*, and *Col1a1* quantified using quantitative reverse transcription polymerase chain reaction after 3 days of culture. (B) Protein expression and semi-quantitative analysis of RUNX2, OCN, and COL1 determined using Western blotting. (C) ALP activity of BMSCs cultured on scaffolds for 7 days. (D) ALP staining and (E) Alizarin red staining with corresponding quantitative analysis. *p<0.05, **p<0.01, ***p<0.001, and ****p<0.0001.

Abbreviations: ALP: Alkaline phosphatase; BMP-2: Bone morphogenetic protein-2; BMSC: Bone marrow stromal cell; N-BTCP: Non-piezoelectric barium titanate/tricalcium phosphate; OD: Optical density; P-BTCP: Piezoelectric barium titanate/tricalcium phosphate; rhBMP-2: Recombinant human bone morphogenetic protein-2.

(**Figure 8A**). To evaluate the newly regenerated bone tissue within the defects, micro-computed tomography analysis was performed, and the results are shown in **Figures 8B** and S4. All scaffolds were well integrated with the host bone, and no pathological abnormalities were observed in H&E staining of major organs (Figure S5), indicating the excellent biocompatibility of the composite scaffolds. In the control group (non-implanted), negligible bone formation was observed throughout the healing period. However, after 8 weeks of implantation, significant cortical bone regeneration was observed in the scaffold-implanted groups, particularly in P-BTCP/BMP-2, where the newly formed bone tissue bridged the defect and completely covered the scaffold pores. After implantation for 12 weeks, the defects were fully covered with new bone in all scaffold-implanted groups. Moreover, P-BTCP/BMP-2 showed superior bone regeneration efficacy, resulting in maximal osseous tissue formation.

Bone mineral density (BMD), the percentage of bone volume to tissue volume (BV/TV), and trabecular thickness (Tb.Th) were quantitatively analyzed, as shown in **Figure 8C**. The mean BMD in P-BTCP/BMP-2 reached 0.37 ± 0.02 g cm^{-3} after 4 weeks, which is approximately 3.5 times higher than that in the control group. After 12 weeks, P-BTCP/BMP-2 exhibited the highest BMD (0.81 ± 0.25 g cm^{-3}), revealing superior bone regeneration and substantial formation of mature bone tissue. Meanwhile, BV/TV demonstrated significantly higher regenerated bone tissue in all scaffold-implanted groups than

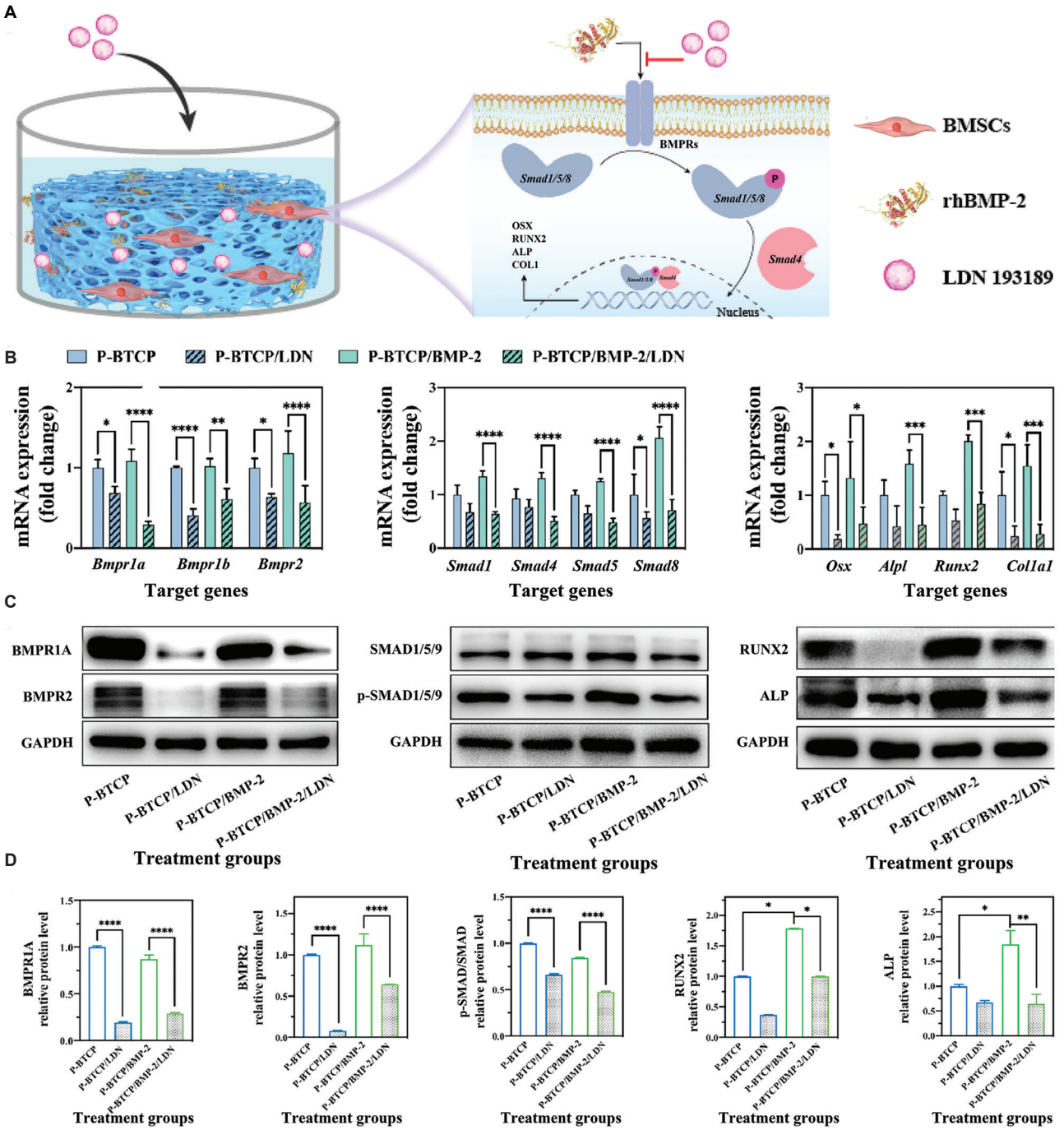

Figure 7. Osteoinductive profiles of BTCP/BMP-2 scaffolds following LDN 193189 treatment. (A) BMSCs were treated with LDN 193189 to inhibit BMPR expression and suppress the BMP/Smad signaling pathway. (B) Gene expression of *Bmpr1a*, *Bmpr1b*, *Bmpr2*, *Smad*, *Osx*, *Alpl*, *Runx2*, and *Col1a1* quantified using quantitative reverse transcription polymerase chain reaction after 3 days of culture. (C) Osteogenic protein expression levels and (D) corresponding semi-quantitative analysis of BMPR1A, BMPR2, SMAD1, SMAD5, SMAD9, RUNX2, and ALP assessed using Western blotting after 3 days of culture. *p<0.05, ** p<0.01, ***p<0.001, and ****p<0.0001.

Abbreviations: BMP-2: Bone morphogenetic protein-2; BMSC: Bone marrow stromal cell; N-BTCP: Non-piezoelectric barium titanate/tricalcium phosphate; P-BTCP: Piezoelectric barium titanate/tricalcium phosphate; rhBMP-2: Recombinant human bone morphogenetic protein-2.

in the control group. Importantly, BV/TV in the P-BTCP/BMP-2 group (32.05 ± 3.18%) was significantly greater than that in the control group (16.70 ± 2.30%) and N-BTCP group (20.12 ± 3.12%) after 12 weeks.

Trabecular bone plays a crucial role in forming irregular 3D networks within the marrow cavity while supporting hematopoiesis. In addition, analyzing the microstructure of trabecular bone is essential for assessing bone regeneration.[35] The P-BTCP/BMP-2 group displayed the maximal Tb.Th values generally indicate that bone anabolism is more prominent than bone catabolism. Similar results were observed in new bone formation rates, with a rate of 2.91%

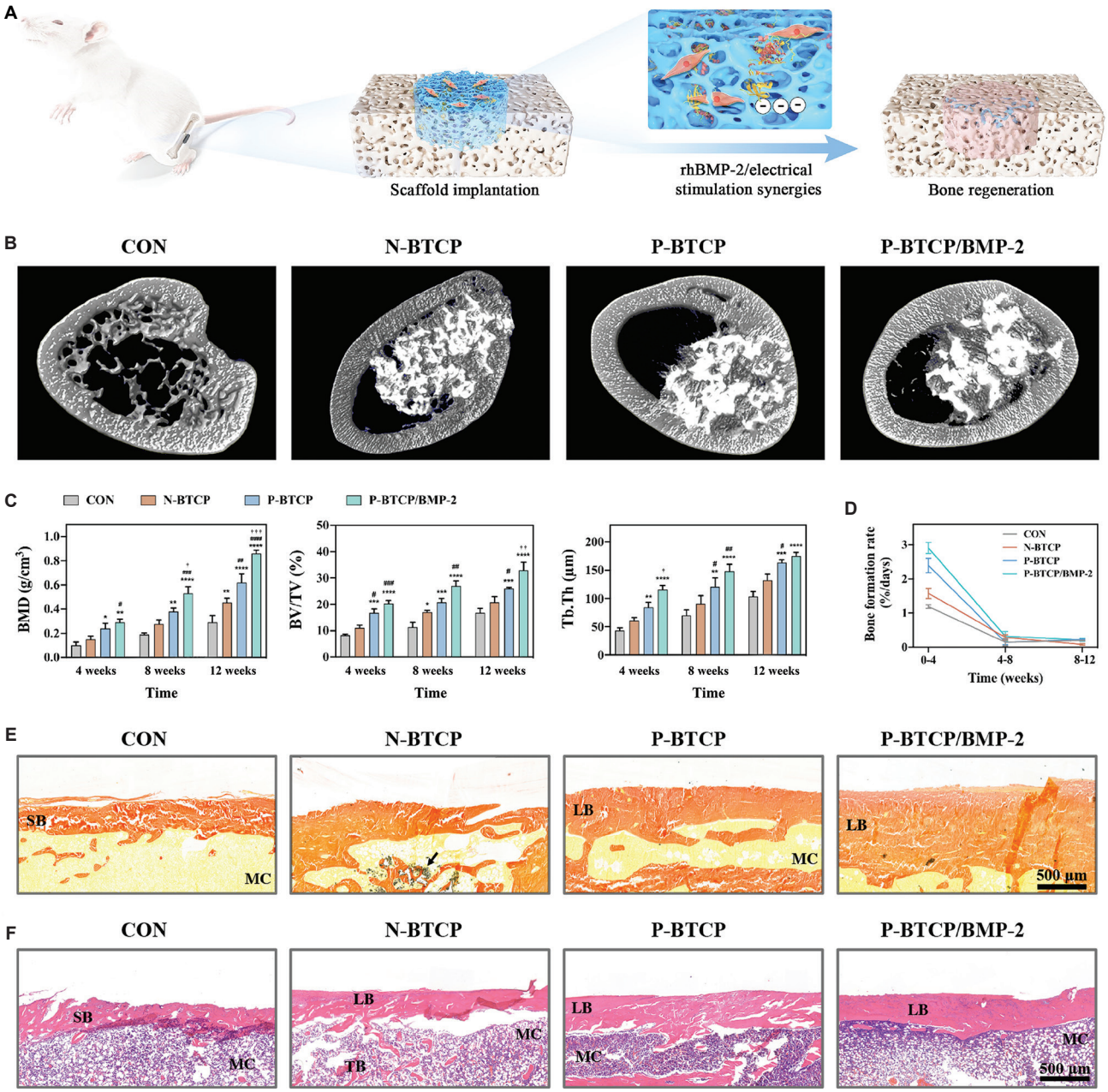

Figure 8. *In vivo* bone formation of BTCP-based scaffolds in a Sprague–Dawley rat femur defect model. (A) Schematic illustration of *in vivo* bone regeneration. (B) Representative three-dimensional micro-computed tomography images of defects 12 weeks post-implantation. (C) BMD, BV/TV, Tb.Th, and (D) bone formation rate at 4, 8, and 12 weeks post-implantation. (E) Van Gieson and (F) hematoxylin–eosin staining of regenerated bone after 12 weeks, with black arrow indicating residual scaffolds (scale bar: 500 μm; magnification: 20×). Statistical significance: $^{*}p<0.05$, $^{**}p<0.01$, $^{***}p<0.001$, and $^{****}p<0.0001$ (vs. CON); $^{\#}p<0.05$, $^{\#\#}p<0.01$, and $^{\#\#\#}p<0.001$ (vs. N-BTCP); and $^{\dagger}p<0.05$, $^{\dagger\dagger}p<0.01$, and $^{\dagger\dagger\dagger}p<0.001$ (vs. P-BTCP).

Abbreviations: BMP-2: Bone morphogenetic protein-2; CON: Control; LB: Lamellar bone; MC: Medullary cavity; N-BTCP: Non-piezoelectric barium titanate/tricalcium phosphate; P-BTCP: Piezoelectric barium titanate/tricalcium phosphate; rhBMP-2: Recombinant human bone morphogenetic protein-2; SB: Spongy bone; TB: Trabecular bone.

in the P-BTCP/BMP-2 group over 4 weeks post-operation, approximately twice that of the control group (1.18%) and N-BTCP group (1.58%) (**Figure 8D**). Therefore, the P-BTCP/BMP-2 scaffolds demonstrated the most favorable bone regeneration outcome, which may be attributed to enhanced osteogenic mineralization and osteoinductive activity. On one hand, the electrical microenvironment exerted by piezoelectric P-BTCP scaffolds promoted mineralized deposition and bone formation. On the other hand, the sustained release of rhBMP-2 induced osteogenic differentiation of stem cells and enhanced osseointegration. Moreover, the synergistic effects of the electrical microenvironment and rhBMP-2 further accelerated bone repair. Consequently, P-BTCP/BMP-2 scaffolds demonstrated promising potential in promoting new bone formation and improving the efficiency of bone regeneration.

The histological assessments of the bone tissues were performed through VG and H&E staining. VG staining of hard tissue slices allows better visualization of the interface between bone tissue and implanted scaffolds (**Figures 8E** and S6). In the control group, a thin layer of spongy bone and partially healed bone formation were observed on the periphery of defects after implantation for 12 weeks. In contrast, more new spongy bone and lamellar bone were observed within the interior of all scaffold groups, suggesting a relatively satisfactory osteoconductive property. The P-BTCP/BMP-2 group exhibited a thicker new bone layer than the N-BTCP and P-BTCP groups. It is worth noting that fewer residual scaffold fragments were observed in the P-BTCP/BMP-2 group after 12 weeks, and the amount and maturity of new lamellar bone were markedly greater, indicating superior osteoinductivity of P-BTCP/BMP-2 scaffolds.

Moreover, H&E staining was employed to further investigate the bone repair capability of P-BTCP/BMP-2 scaffolds (**Figures 8F** and S7). In the control group, the bone defect was filled with a large amount of fibrous tissue, with a few trabeculae present in the middle of the defect region during the first 4 weeks. After 12 weeks, only a few newly formed spongy bone tissues were observed over the fibrotic tissue. In contrast, regenerated bone tissue appeared within the initial 4 weeks in scaffold-implanted groups, and the conversion of spongy bone to lamellar bone gradually increased over the subsequent 8 weeks. Notably, a large quantity of spongy bone was generated even in the P-BTCP and P-BTCP/BMP-2 groups after 4 weeks. In comparison with the P-BTCP group, the thickness of the formed bone tissue was relatively greater in the P-BTCP/BMP-2 group, and the defect area was almost covered with newly formed bone tissue. Taken together, these findings likely result from the excellent osteogenic mineralization of the piezoelectric P-BTCP scaffolds and the enhanced pro-osteogenesis activity of rhBMP-2 mediated by the electrical microenvironment on P-BTCP.

4. Conclusions

Electroactive porous P-BTCP scaffolds loaded with rhBMP-2 were successfully fabricated to synergistically enhance bone repair through piezoelectric stimulation through BMPR activation. The piezoelectric stimulation from P-BTCP scaffolds effectively promoted the early adhesion, proliferation, and migration of BMSCs. Meanwhile, piezoelectric signals facilitated the formation of surface mineralized apatite layers, making a significant contribution to cell–material interactions and osteogenic differentiation of BMSCs. Owing to relatively strong electrostatic interactions, the 3D porous P-BTCP scaffolds achieved efficient immobilization (twice as high as that of N-BTCP) and sustained release of rhBMP-2, thereby prolonging its osteogenic effect. Moreover, the results demonstrate that P-BTCP scaffolds increased the expression of BMPRs by approximately three-fold. This significant increase in BMPR expression enhanced the affinity for rhBMP-2, promoting the binding process and the subsequent activation of downstream osteogenic signaling pathways. These rhBMP-2–loaded piezoelectric scaffolds synergistically accelerate osteogenesis in a rat femur model. This study provides valuable insights for further innovation in the design and development of growth factor-loaded piezoplatforms for tissue repair.

Acknowledgement

The authors would like to thank the Research Center of Analysis and Test, East China University of Science and Technology, for their assistance in the characterization works.

Financial support

This study was supported by the National Natural Science Foundation of China (32471407, 32171342), the National Key Research and Development Program of China (2023YFC2413600), the Shanghai Pujiang Program (16PJD015), the Joint Fund for Equipment Pre-research of the Ministry of Education (6141A02022618), and the IER Foundation 2021 (IERF202103).

Conflicts of interest statement

The authors declare no conflicts of interest.

Author contributions

Conceptualization: FC and LM; *Formal analysis*: LM and DZ; *Methodology*: XW and CL; *Investigation*: LM and ZS; *Software:* DZ; *Writing–original draft*: LM; *Writing–review & editing*: FC and CL. All authors have read and agreed to the published version of the manuscript.

Ethics approval and consent to participate

This work has been approved by the local ethics committee: Animal Ethics Committee of East China University of Science and Technology (ECUST-21046). This work did not involve human patients.

Consent for publication

Not applicable.

Availability of data

Data are available from the corresponding author upon reasonable request.

References

1. Zhang Q, Liu Y, Li J, Wang J, Liu C. Recapitulation of growth factor-enriched microenvironment via BMP receptor activating hydrogel. *Bioact Mater.* 2023;20:638-650. doi: 10.1016/j.bioactmat.2022.06.012
2. Wang CK, Ho ML, Wang GJ, *et al.* Controlled-release of rhBMP-2 carriers in the regeneration of osteonecrotic bone. *Biomaterials.* 2009;30:4178-4186. doi: 10.1016/j.biomaterials.2009.04.029
3. Lee HY, Kim DS, Hwang GY, *et al.* Multi-modulation of immune-inflammatory response using bioactive molecule-integrated PLGA composite for spinal fusion. *Mater Today Bio.* 2023;19:100611. doi: 10.1016/j.mtbio.2023.100611
4. Krishnan L, Priddy LB, Esancy C, *et al.* Delivery vehicle effects on bone regeneration and heterotopic ossification induced by high dose BMP-2. *Acta Biomater.* 2017;49:101-112. doi: 10.1016/j.actbio.2016.12.012
5. Tian X, Vater C, Raina DB, *et al.* Co-delivery of rhBMP-2 and zoledronic acid using calcium sulfate/hydroxyapatite carrier as a bioactive bone substitute to enhance and accelerate spinal fusion. *Bioact Mater.* 2024;36:256-271. doi: 10.1016/j.bioactmat.2024.02.034
6. Liu W, Liu C, Liu C, *et al.* Surface chemical modification of poly(phthalazinone ether nitrile ketone) through rhBMP-2 and antimicrobial peptide conjugation for enhanced osteogenic and antibacterial activities *in vitro* and *in vivo*. *Chem Eng J.* 2021;424:130321. doi: 10.1016/j.cej.2021.130321
7. Chen X, Tan B, Bao Z, *et al.* Enhanced bone regeneration via spatiotemporal and controlled delivery of a genetically engineered BMP-2 in a composite hydrogel. *Biomaterials.* 2021;277:121117. doi: 10.1016/j.biomaterials.2021.121117

8. Yu Y, Chen R, Yuan Y, Wang J, Liu C. Affinity-selected polysaccharide for rhBMP-2-induced osteogenesis via BMP receptor activation. *Appl Mater Today*. 2020;20:100681. doi: 10.1016/j.apmt.2020.100681
9. Wei H, Cui J, Lin K, Xie J, Wang X. Recent advances in smart stimuli-responsive biomaterials for bone therapeutics and regeneration. *Bone Res*. 2022;10(1):17. doi: 10.1038/s41413-021-00180-y
10. Li Y, Xiao Y, Liu C. The horizon of materiobiology: A perspective on material-guided cell behaviors and tissue engineering. *Chem Rev*. 2017;117(5):4376. doi: 10.1021/acs.chemrev.6b00654
11. Zhang Y, Khanbareh H, Dunn S, *et al*. High efficiency water splitting using ultrasound coupled to a BaTiO3 nanofluid. *Adv Sci (Weinh)*. 2022;9(9):2105248. doi: 10.1002/advs.202105248
12. Zhou X, Wu S, Li C, *et al*. Piezophototronic effect in enhancing charge carrier separation and transfer in ZnO/BaTiO3 heterostructures for high-efficiency catalytic oxidation. *Nano Energy*. 2019;66:104127. doi: 10.1016/j.nanoen.2019.104127
13. Xu Q, Gao X, Zhao S, *et al*. Construction of bio-piezoelectric platforms: From structures and synthesis to applications. *Adv Mater*. 2023;3(27):2008452. doi: 10.1002/adma.202008452
14. Mao L, Bai L, Wang X, *et al*. Enhanced cell osteogenesis and osteoimmunology regulated by piezoelectric biomaterials with controllable surface potential and charges. *ACS Appl Mater Inter*. 2022;14(39):44111-44124. doi: 10.1021/acsami.2c11131
15. Wu H, Dong H, Tang Z, *et al*. Electrical stimulation of piezoelectric $BaTiO_3$ coated Ti6Al4V scaffolds promotes anti-inflammatory polarization of macrophages and bone repair via MAPK/JNK inhibition and OXPHOS activation. *Biomaterials*. 2023;293:121990. doi: 10.1016/j.biomaterials.2022.121990
16. MaoL, Yin Y, Zhang L, *et al*. Regulation of inflammatory response and osteogenesis to citrate-based biomaterials through incorporation of alkaline fragments. *Adv Healthc Mater*. 2022;11(4):2101590. doi: 10.1002/adhm.202101590
17. De Wildt BW, Van der Meijden R, Bartels PA, *et al*. Bioinspired silk fibroin mineralization for advanced *in vitro* bone remodeling models. *Adv Funct Mater*. 2022;32(41):2206992. doi: 10.1002/adfm.202206992
18. Gooding S, Olechnowicz SW, Morris EV, *et al*. Transcriptomic profiling of the myeloma bone-lining niche reveals BMP signalling inhibition to improve bone disease. *Nat Commun*. 2019;10(1):4533. doi: 10.1038/s41467-019-12296-1
19. Liu Y, Ma Y, Zhang J, *et al*. MBG-modified β-TCP scaffold promotes mesenchymal stem cells adhesion and osteogenic differentiation via a FAK/MAPK signaling pathway. *ACS Appl Mater Inter*. 2017;9(36):30283-30296. doi: 10.1021/acsami.7b02466
20. Caballero AC, Fernández JF, Villegas M, *et al*. Intermediate phase development in phosphorus-doped barium titanate. *J Am Ceram Soc*. 2000;83(6):1499-1505. doi: 10.1111/j.1151-2916.2000.tb01417.x
21. Khare D, Basu B, Dubey AK. Electrical stimulation and piezoelectric biomaterials for bone tissue engineering applications. *Biomaterials*. 2020;258:120280. doi: 10.1016/j.biomaterials.2020.120280
22. Polley C, Distler T, Detsch R, *et al*. 3D printing of piezoelectric barium titanate-hydroxyapatite scaffolds with interconnected porosity for bone tissue engineering. *Materials (Basel)*. 2020;13:1773. doi: 10.3390/ma13071773
23. Shao CS, Chen LJ, Tang RM, Zhang B, Tang JJ, Ma WN. Polarized hydroxyapatite/$BaTiO_3$ scaffolds with bio-inspired porous structure for enhanced bone penetration. *Rare Met*. 2022;41(1):67-77. doi: 10.1007/s12598-021-01798-x
24. Kim HM, Himeno T, Kokubo T, Nakamura T. Process and kinetics of bonelike apatite formation on sintered hydroxyapatite in a simulated body fluid. *Biomaterials*. 2005;26(21):4366-4373. doi: 10.1016/j.biomaterials.2004.11.022
25. Metwally S, Stachewicz U. Surface potential and charges impact on cell responses on biomaterials interfaces for medical applications. *Mater Sci Eng C*. 2019;104:109883. doi: 10.1016/j.msec.2019.109883
26. Santoni BL, Niggli L, Dolder S, *et al*. Effect of minor amounts of β-calcium pyrophosphate and hydroxyapatite on the physico-chemical properties and osteoclastic resorption of β-tricalcium phosphate cylinders. *Bioact Mater*. 2022;10:222-235. doi: 10.1016/j.bioactmat.2021.09.003
27. Kapat K, Shubhra QT, Zhou M, Leeuwenburgh S. Piezoelectric nano-biomaterials for biomedicine and tissue regeneration. *Adv Funct Mater*. 2020;30(44):1909045. doi: 10.1002/adfm.201909045
28. Zhou HX, Pang X. Electrostatic interactions in protein structure, folding, binding, and condensation. *Chem Rev*. 2018;118(4):1691-1741. doi: 10.1021/acs.chemrev.7b00305
29. Yu X, Lin F, Li P, *et al*. Porous scaffolds with enzyme-responsive Kartogenin release for recruiting stem cells and promoting cartilage regeneration. *Chem Eng J*. 2022;447:137454. doi: 10.1016/j.cej.2022.137454
30. Lee SS, Hsu EL, Mendoza M, *et al*. Gel scaffolds of BMP-2-binding peptide amphiphile nanofibers for spinal arthrodesis. *Adv Healthc Mater*. 2015;4(1):131-141. doi: 10.1002/adhm.201400129
31. Xiang H, Yang Q, Gao Y, *et al*. Cocrystal strategy toward multifunctional 3D-printing scaffolds enables NIR-activated photonic osteosarcoma hyperthermia and enhanced bone defect regeneration. *Adv Funct Mater*. 2020;30(25):1909938. doi: 10.1002/adfm.201909938
32. Zhang L, Yang G, Johnson BN, Jia X. Three-dimensional (3D) printed scaffold and material selection for bone repair. *Acta Biomater*. 2019;84:16-33. doi: 10.1016/j.actbio.2018.11.039
33. Cui L, Zhang J, Zou J, *et al*. Electroactive composite scaffold with locally expressed osteoinductive factor for synergistic bone repair upon electrical stimulation. *Biomaterials*. 2020;230:119617. doi: 10.1016/j.biomaterials.2019.119617
34. Huang RL, Chen G, Wang W, *et al*. Synergy between IL-6 and soluble IL-6 receptor enhances bone morphogenetic protein-2/absorbable collagen sponge-induced bone regeneration via regulation of BMPRIA distribution and degradation. *Biomaterials*. 2015;67:308-322. doi: 10.1016/j.ebiom.2016.09.016
35. Cervantes M, Lal A, Marsh AM, Fung EB. Assessing bone quality using trabecular bone score in patients with hemoglobinopathies. *Blood*. 2016;128(22):3629. doi: 10.1182/blood.V128.22.3629.3629

Received: April 25, 2025
Revised: October 23, 2025
Accepted: October 26, 2025
Available online: December 18, 2025